nature catalysis



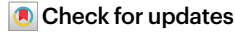
Article

https://doi.org/10.1038/s41929-025-01436-0

De novo design and evolution of an artificial metathase for cytoplasmic olefin metathesis

Received: 17 January 2025

Accepted: 2 October 2025



Zhi Zou ♠ ^{1,2,6}, Indrek Kalvet ♠ ^{3,4,5,6}, Boris Lozhkin ♠ ^{1,6}, Elinor Morris ¹, Kailin Zhang ¹, Dongping Chen ♠ ¹, Marco L. Ernst ♠ ¹, Xiang Zhang ♠ ¹, David Baker ♠ ^{3,4,5} ⋈ & Thomas R. Ward ♠ ^{1,2} ⋈

Artificial metalloenzymes present a promising avenue for abiotic catalysis within living systems. However, their in vivo application is currently limited by critical challenges, particularly in selecting suitable protein scaffolds capable of binding abiotic cofactors and maintaining catalytic activity in complex media. Here we address these limitations by introducing an artificial metathase—an artificial metalloenzyme designed for ring-closing metathesis—for whole-cell biocatalysis. Our approach integrates a tailored metal cofactor into a hyper-stable, de novo-designed protein. By combining computational design with genetic optimization, a binding affinity ($K_D \le 0.2 \,\mu\text{M}$) between the protein scaffold and cofactor is achieved through supramolecular anchoring. Directed evolution of the artificial metathase yielded variants exhibiting excellent catalytic performance (turnover number $\ge 1,000$) and biocompatibility. This work represents a pronounced leap in the de novo design and in cellulo engineering of artificial metalloenzymes, paving the way for abiological catalysis in living systems.

Enzymes are gaining acceptance among the synthetic community, thanks to their catalytic benefits with regard to sustainability, step economy and exquisite selectivity^{1,2}. Stimulated by these attractive features, efforts are underway to expand the catalytic repertoire of enzymes by designing artificial metalloenzymes (ArMs), which harbour a synthetic metal catalyst within a protein and catalyse newto-nature reactions. Strategies for assembling ArMs rely on either substituting native metals/cofactors within native active sites³⁻⁷ or anchoring synthetic organometallic complexes into proteins. Such anchoring can be achieved either via covalent⁸⁻¹², dative¹³⁻¹⁶ or supramolecular interactions¹⁷⁻¹⁹ between the cofactor and the protein. Although these strategies have proven fruitful both in homogenous^{8,14,20} and heterogenous systems^{21,22}, the protein environment surrounding the cofactor—which substantially influences catalytic performance²³⁻²⁵—is by-and-large dictated by the anchoring moiety and thus may be incompatible with the ArM's intended function. Accordingly, such ArMs often require further engineering efforts to improve their catalytic performance 15,26. An additional challenge of ArMs is the modest compatibility of many synthetic cofactors with the complex whole-cell environment ²⁷⁻³⁰. Accommodating and shielding these cofactors within a protein may offer a hospitable environment by minimizing (bimolecular) decomposition as well as inactivation by water and nucleophilic cell metabolites, such as glutathione (hereafter GSH)^{19,25}. Over the past decade, notable progress has been achieved in expanding the scope of in cellulo biotransformations catalysed by ArMs, incorporating diverse metal cofactors including copper-³¹, gold-²⁰, iridium-³²⁻³⁶, ruthenium-^{37,38} and rhodium-based cofactors ³⁹ (Supplementary Table 1). Despite these advances, most ArMs reported to date display only modest enhancements in catalytic performance—typically assessed by their turnover number (TON)—compared with their wild-type counterparts. Notable exceptions include a handful of highly active [Ir(Me)MPIX]-based systems, that catalyse carbene insertion³³ or cyclopropanation³⁴.

Olefin metathesis is a powerful and widely used transformation in organic synthesis and materials science, enabling the efficient and selective formation of carbon–carbon double bonds⁴⁰. However,

¹Department of Chemistry, University of Basel, Basel, Switzerland. ²National Center of Competence in Research 'Molecular Systems Engineering', Basel, Switzerland. ³Department of Biochemistry, University of Washington, Seattle, WA, USA. ⁴Institute for Protein Design, University of Washington, Seattle, WA, USA. ⁵Howard Hughes Medical Institute, University of Washington, Seattle, WA, USA. ⁶These authors contributed equally: Zhi Zou, Indrek Kalvet, Boris Lozhkin. —e-mail: dabaker@uw.edu; thomas.ward@unibas.ch

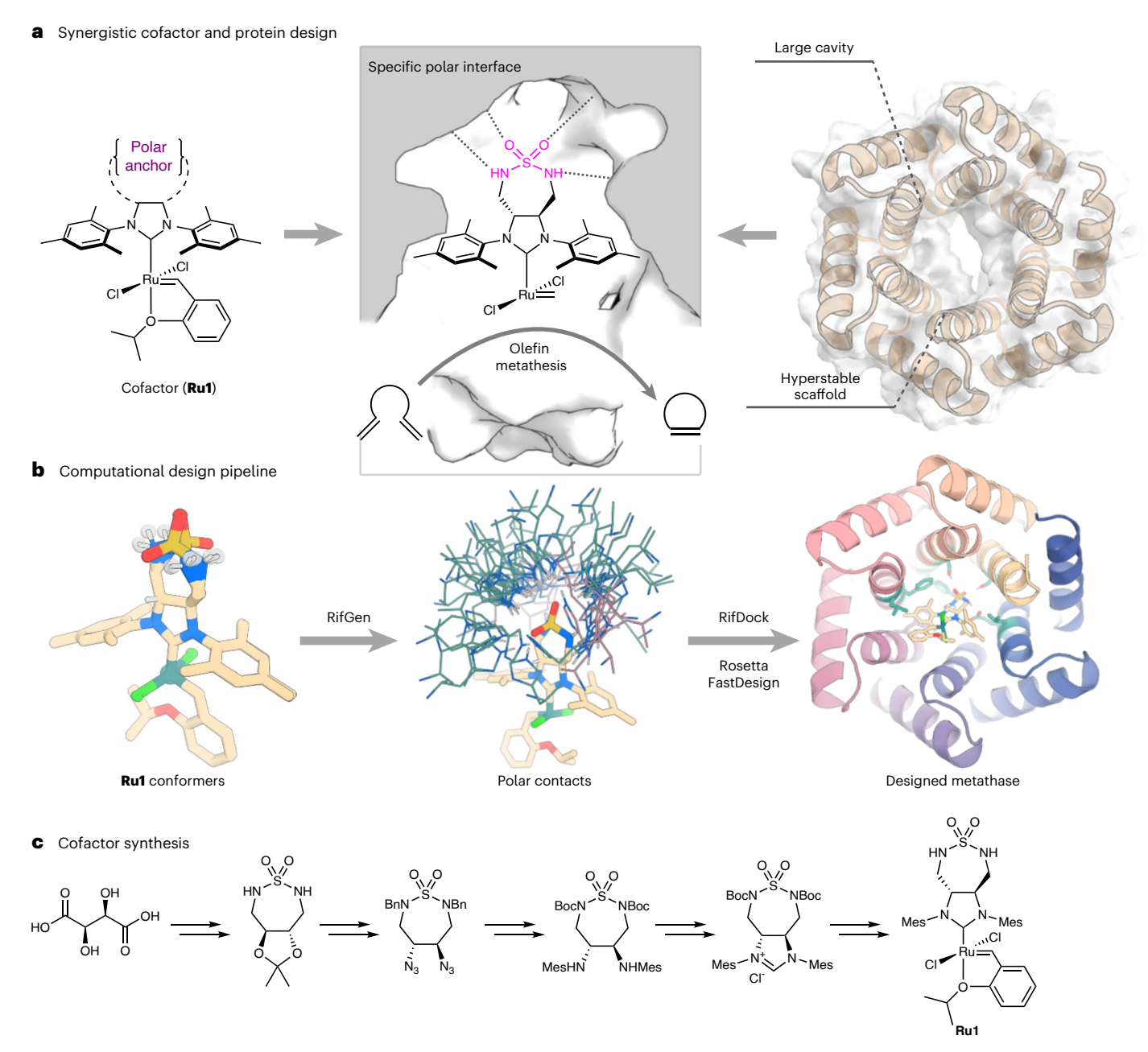


Fig. 1 | Creation of a de novo artificial metathase through synergistic cofactor and protein design. a, Modification of the Hoveyda–Grubbs second-generation olefin metathesis catalyst ($\mathbf{Ru1}$) with a polar sulfamide anchoring group and a de novo-designed protein as binding partner. b, The computational design pipeline consists of generating polar contacts around the ligand using RifGen

(displayed as a cloud of histidine rotamers), placement of the binding motifinto the de novo protein with RifDock and sequence optimization with Rosetta FastDesign. \mathbf{c} , The synthesis of $\mathbf{Ru1}$ from L-(+)-tartaric acid in sixteen steps (see Supplementary Methods for details).

its application in chemical biology remains limited, as poor biocompatibility with cellular components often necessitates the use of (super-)stoichiometric amounts of catalyst to achieve acceptable conversions ^{19,41-45}. To overcome these limitations, we and others have explored the potential of artificial metathases—ArMs capable of catalysing olefin metathesis. These efforts have led to demonstrations of ArM activity in diverse biological environments, including body fluids ^{19,43}, the periplasm ^{37,46}, the cell surface ⁴⁷ and artificial membraneless organelles ⁴⁵ (Supplementary Table 1). Building on this, we hypothesized that a specifically tailored, de novo-designed host protein could provide enhanced tunability and stability, ultimately enabling the development of a best-in-class ArM for olefin metathesis in the cytoplasm of *Escherichia coli*.

We set out to design a Hoveyda–Grubbs olefin metathesis catalyst along with a de novo-designed protein that could house it in a manner optimal for catalysis (Fig. 1a). De novo protein design has matured to a stage where diverse protein scaffolds 48–50 and tailored binding sites for various small molecules can be reliably designed 51–53. We reasoned that these advances could enable us to design a hyper-stable protein that binds a catalytically competent cofactor exclusively via supramolecular interactions. From the catalyst perspective, we sought to address this challenge by designing a derivative of the Hoveyda–Grubbs catalyst (hereafter **Ru1**) that contains a polar motif, aimed at interacting via H-bonds with the protein, as well as improving the cofactor solubility in aqueous media (Fig. 1a). We reasoned that through computational protein design, the binding pocket could be tailored to provide

complementary weak interactions with the cofactor ${\bf Ru1}$. In addition, a hydrophobic pocket to interact with mesityl moieties of the cofactor and to harbour the catalytic event (Fig. 1b). We surmised that such synergistic design of abiotic cofactor and host protein could provide access to a greater variety of ArMs, unconstrained by the compatibility limits of existing systems.

In this study, we achieved this objective by creating an ArM that integrates the synthetic cofactor **Ru1** within a de novo-designed protein scaffold. The resulting artificial metathase catalysed ring-closing metathesis (RCM) of olefins in the cytoplasm of *E. coli*. Through directed evolution, its catalytic performance was substantially optimized (\geq 12-fold). Collectively, these findings demonstrate the feasibility of supramolecular anchoring of synthetic precious-metal cofactors within de novo-designed proteins. This strategy provides a versatile platform for creating and optimizing new-to-nature catalysis in cellulo.

Results

De novo design of host proteins to accommodate Ru1

With the Ru1 catalyst at hand (Fig. 1c), we proceeded with designing proteins to bind to it. Since one of the key features of the catalyst is its polar sulfamide group, we sought to use this moiety as a guide for the computational design efforts. By using the RifGen/RifDock50 suite of programmes we enumerated the interacting amino acid rotamers around the cofactor and docked the ligand with a set of these residues into the cavities of de novo-designed proteins (Fig. 1b). The de novo-designed closed alpha-helical toroidal repeat proteins (such as Protein Data Bank (PDB) ID: 4YXX, hereafter dnTRP) were selected as the protein scaffold, owing to their high thermostability, engineerability and a suitably sized pocket for ligand-binding^{52,54}. Docked structures containing the cofactor Ru1 and the key interacting residues were then subjected to further protein sequence optimization (refining hydrophobic contacts with the ligand and stabilizing the key H-bonding residues) using Rosetta FastDesign⁵⁴. The design models were subsequently evaluated for computational metrics describing the protein-cofactor interface and pre-organization of the binding pocket. This led us to select 21 designs (dnTRP, hereafter) for experimental testing (Supplementary Methods).

Identification of the most promising dnTRP

Each of the 21 dnTRPs, featuring an N-terminal hexa-histidine tag and a TEV protease cleavage sequence, were expressed in *E. coli*. SDS-polyacrylamide gel electrophoresis analysis revealed that 17 of these were expressed mostly in the soluble fraction; these were purified by nickel-affinity chromatography (Supplementary Fig. 2).

To identify the most promising scaffold for RCM, we evaluated the 17 purified dnTRPs treated with **Ru1** (0.05 equivalents (equiv.) versus dnTRP) in the presence of the diallylsulfonamide **1a** (5,000 equiv. versus **Ru1**) as prototypical RCM substrate (Fig. 2a). Under standard RCM conditions (that is 18 h, pH 4.2) all artificial metathases (hereafter **Ru1**-dnTRPs) afforded higher TONs than the free cofactor **Ru1** (TON 40 ± 4), with dnTRP_10, dnTRP_17 and dnTRP_18 performing best (TON 183 ± 19 , 181 ± 7 and 194 ± 6 , respectively) (Fig. 2b). In light of its high expression level, we selected dnTRP 18 for the remainder of the study.

Stability studies of the *apo* dnTRP_18 revealed tolerance towards pH values ranging from 2.6 to 8.0 and a pronounced thermal stability, with a $T_{50} > 98^{\circ}\text{C}$ (T_{50} : temperature at which 50% of the protein is denatured after 30-min incubation; Supplementary Fig. 3), in accordance with previous reports on structurally related dnTRPs⁵⁵. Next, we determined the binding affinity of **Ru1** for dnTRP_18 using a tryptophan fluorescence-quenching assay ($K_D = 1.95 \pm 0.31 \, \mu\text{M}$) (Supplementary Fig. 4). To further improve the affinity and ensure near quantitative binding at low micromolar concentrations of dnTRP_18, we set out to increase the hydrophobicity around the **Ru1** binding site. For this purpose, positions F43 and F116 were individually mutated to tryptophan (Fig. 2c). Both dnTRP 18 F43W and dnTRP 18 F116W

(hereafter dnTRP_R0) displayed a nearly tenfold higher affinity with $K_{\rm D} = 0.26 \pm 0.05$ and 0.16 ± 0.04 µM at pH 4.2, respectively (Fig.2d). Native mass spectrometry and size-exclusion chromatography further highlighted the binding between **Ru1** and dnTRP_R0 and the formation of the **Ru1**·dnTRP_R0 complex with a 1:1 stoichiometry (Supplementary Fig. 5).

Directed evolution of Ru1·dnTRP

Directed evolution is a preeminent methodology for engineering of natural enzymes and ArMs to improve their catalytic performance⁵⁶ To facilitate streamlined engineering of artificial metathases, we sought suitable conditions for the RCM screening using E. coli cell-free extracts (CFE). Based on the **Ru1**·dnTRP ROpH-affinity profile (Fig. 2d), we prepared the CFE at pH 4.2 and supplemented the reaction mixture with bis(glycinato)copper(II) [Cu(Gly)₂]—which had been shown previously to partially oxidize GSH present in cell lysates³⁵—thus enabling screening **Ru1**·dnTRP in CFE (compare 197 ± 7 TON with $[Cu(Gly)_2] = 5$ mM versus 152 ± 16 TON in untreated CFE) (Supplementary Fig. 6a). To reflect the typical dnTRP concentrations obtained in the CFE from a 1 ml culture in a 96-well plate, we set [**Ru1**] = $0.5 \,\mu\text{M}$, thus ensuring its near-quantitative binding to dnTRPs (Supplementary Figs. 6b and 7). Relying on this protocol, we established a high-throughput endpoint screening assay in a 96-well plate format for the directed evolution of Rul·dnTRP, starting from Rul·dnTRP_RO (hereafter Rul·RO) (Supplementary Fig. 8a). The first three rounds of directed evolution involved screening iterative site-saturation mutagenesis (SSM) libraries by targeting amino acid residues in the proximity of the computed position of **Ru1**. Following the screening using CFE, the most promising variants were validated with purified dnTRPs. The most promising mutants for each round are abbreviated as Ru1·R1 (that is, Ru1·dnTRP 18 F43R/ F116W, TON 319 ± 34), Ru1·R2 (that is, Ru1·dnTRP_18_E4G/F43R/F116W, TON 379 \pm 8) and Ru1·R3 (that is Ru1·dnTRP 18 E4G/F43R/F116W/ E144G, TON 412 ± 6) (Supplementary Fig. 8b-e). For the fourth round, we screened an error-prone PCR (epPCR) library (1,800 colonies) relying on Ru1·R3 and identified Ru1·R4 (that is, Ru1·dnTRP 18 E4G/F43R/ I44T/F116W/E144G/E179G) with 2.6-fold and 43-fold increased TON over **Ru1**·RO and **Ru1**, respectively (Supplementary Fig. 8f,g). For the fifth round, we screened a fragment shuffling library (540 colonies) by randomly recombining the beneficial mutations from third and fourth rounds (Supplementary Fig. 8h). This led to the identification of variant Ru1·R5 (that is, Ru1·dnTRP 18 E4G/F43R/I44T/F116W/A119V/ E144G/E179G/K206T) that afforded TON = 339 \pm 34 and 570 \pm 25 in CFE and purified form, respectively (Fig. 3a).

With this evolved variant at hand, we evaluated the metathase's performance at higher pH values, with the ultimate goal of performing RCM in E, coli whole cells. The performance of Ru-based metathesis catalysts in aqueous solution is negatively impacted by basic media^{27,59}. To evaluate the effect of the directed evolution on the pH-dependent metathase activity of **Ru1**-dnTRPs, we compared the performance of **Ru1**-R5 with that of **Ru1** and **Ru1**-R0 at various pHs (Fig. 3b). Gratifyingly, the pH-tolerance along the evolutionary trajectory closely follows the TON trends: **Ru1**-R5 > **Ru1**-R0 > **Ru1**, highlighting the beneficial effect of the dnTRP scaffold and the directed evolution trajectory. The evolved metathase **Ru1**-R5 maintained nearly half of its activity at pH 6.0 (versus pH 4.2), whereas **Ru1**-R0 lost nearly ninety percent of its activity. Only traces of the product **2a** (for example, TON \leq 10) were detected at pH \geq 5.2 in the presence of the free cofactor **Ru1** (Fig. 3b).

Evaluation of the catalytic performance of the Ru1·dnTRPs with purified samples

To evaluate the effect of the N-terminal his-tag on both catalytic performance and cofactor affinity, we removed it via TEV protease cleavage (hereafter dnTRP- Δ His). Removal of His-tag resulted in lower K_D value at pH 6.0 (Fig. 2d versus Supplementary Fig. 10a). We surmise

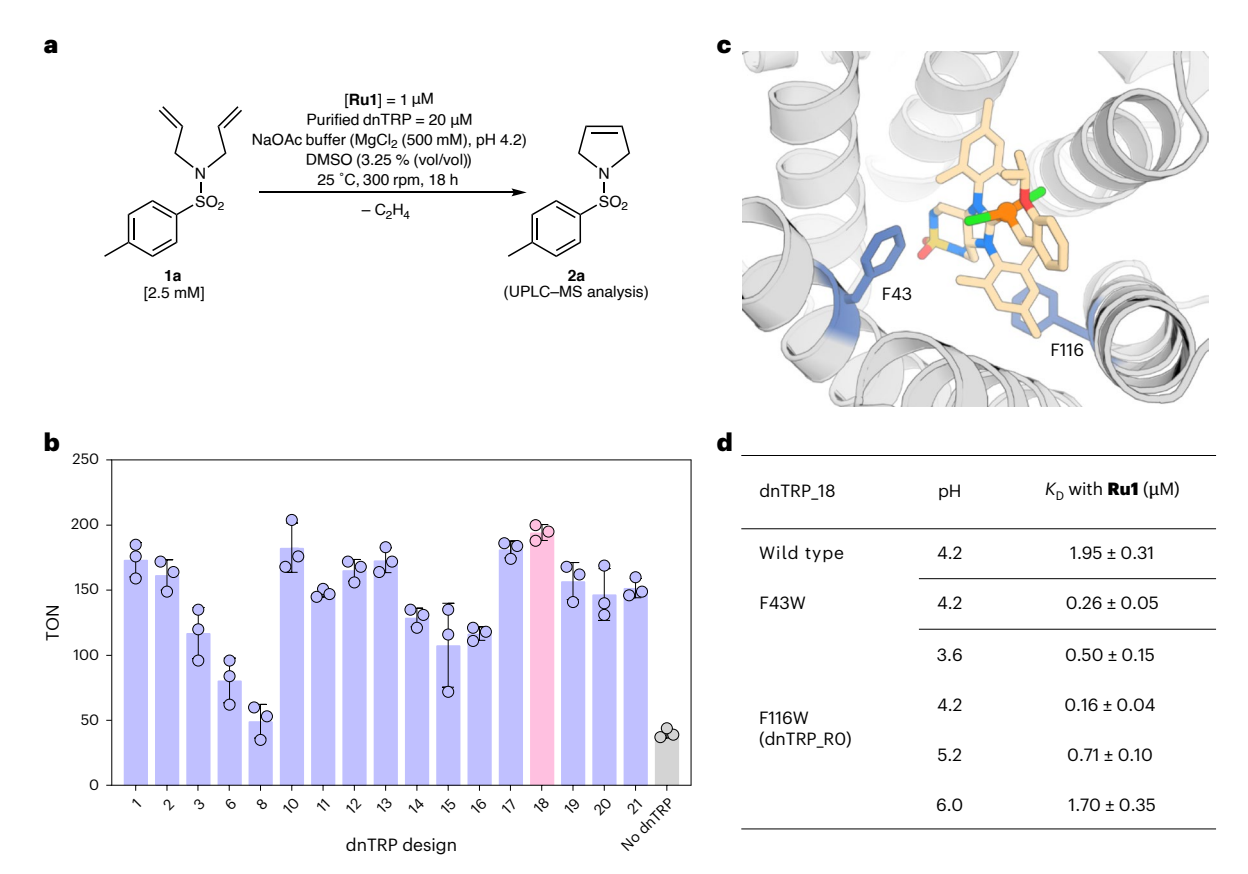


Fig. 2 | **Selection and optimization of dnTRPs for assembly of Ru1-dnTRPs. a**, Substrate **1a** and RCM reaction conditions using purified dnTRPs. **b**, The catalytic performance (TON) for the RCM of substrate **1a** in the presence of the **Ru1**-dnTRP using the 17 dnTRPs as host proteins. The data are displayed as mean values of three replicates with error bars indicating standard deviations (n = 3). **c**, A computed model of dnTRP_18 highlighting two residues F43 and F116 (blue sticks), which were individually mutated to tryptophan to increase hydrophobicity around the **Ru1** cofactor. The **Ru1** cofactor (colour-coded

sticks) and the ruthenium atom (orange sphere) are displayed. **d**, A summary of the binding affinity (K_D) of **Ru1** for dnTRP_18 and single mutants thereof at various pHs. The data are displayed as mean values of three replicates \pm standard deviation (n=3). The replicates for **b** and **d** were independently performed using the same stock of purified dnTRPs. The tryptophan fluorescence-quenching assay and the fitting procedure to derive the K_D are presented in the Supplementary Methods and Supplementary Fig. 4.

that removal of His-tag may minimize undesirable interactions with Ru1 (pH 6.0) and thus contributes to lower the K_D . The corresponding dnTRP- Δ His variants proved more active than the variants containing the Lewis-basic affinity tag, especially at a higher pH (Fig. 3b). We then evaluated the effect of both temperature and pH on the RCM's activity. The highest TON was achieved at 50 °C. At pH 3.6 and 50 °C, **Ru1**-R5- Δ His afforded a TON of 1,028 \pm 159 (Fig. 3b). Notably, **Ru1**-dnTRPs retain \geq 40% activity at 90 °C at both pH 4.2 and 6.0 (Supplementary Fig. 11a). Unfortunately, all attempts to express dnTRP- Δ His in *E. coli* lead to markedly lower yields, thus challenging its use in *E. coli* whole-cell studies (Supplementary Fig. 10b).

To assess the substrate scope of the $\mathbf{Ru1}$ -dnTRPs, five dienes, one triene and one enyne substrate were tested in the presence of $\mathbf{Ru1}$, $\mathbf{Ru1}$ -R0- Δ His and $\mathbf{Ru1}$ -R5- Δ His (Fig. 3c and Supplementary Fig. 12). Comparison of the RCM performance highlights that the $\mathbf{Ru1}$ -dnTRPs accept various substrates, leading to substantially improved TONs compared with the free cofactor $\mathbf{Ru1}$. Except for substrate $\mathbf{1e}$, the fifth generation variant $\mathbf{Ru1}$ -R5- Δ His lead to improved TONs compared to $\mathbf{Ru1}$ -R0- Δ His. The presence of an ammonium group on the diene $\mathbf{1b}$, nearly completely shuts down RCM activity, both for the free cofactor $\mathbf{Ru1}$ and for the $\mathbf{Ru1}$ -dnTRPs. No enantioselectivity was observed for the RCM of the prochiral triene $\mathbf{1c}$.

Structural characterization of Ru1·dnTRPs

We obtained X-ray crystal structures of *apo* dnTRP_RO-ΔHis (resolved to 1.6 Å, PDB: 9GVF), *holo* **Ru1**·RO-ΔHis (resolved to 2.9 Å, PDB: 8S6P)

and **Ru1**·R5-ΔHis (resolved to 2.9 Å, PDB: 9H3C). A comparison of apo and **Ru1**·dnTRP RO-ΔHis X-ray structures with computational models reveals an overall agreement with the toroidal shape but notable deviations with regards to the shape of the inner cavity, as well as the position the Ru1 cofactor. Specifically, the X-ray structure of **Ru1**·RO-ΔHis reveals a cylindrical pocket, in contrast to the conical shape predicted for $\textbf{Ru1}\cdot \text{RO-}\Delta \text{His}$ and $\textbf{Ru1}\cdot \text{dnTRP_}18$ with AlphaFold2 (AF2)⁶⁰. The $C\alpha$ root mean square deviation values between the AF2 predicted models and the X-ray structures range from 1.59 to 1.63 Å (Fig. 4a and Supplementary Fig. 13a,b). The ruthenium's position in the **Ru1**·RO-ΔHis X-ray structure (as judged from the ruthenium's anomalous density) is shifted by 3.4 Å compared with the **Ru1**·dnTRP_18 model (Supplementary Fig. 13c). Consequently, compared with the AF2 model, the TRP amino acid side chains that interact with the cofactor Ru1 differ. The residues predicted by AF2 to interact with **Ru1** include S11, S46, Y50 and E186 as primary contributors. Instead, the X-ray structure reveals the closest contacts between residues Y50 and K190 with sulfamide anchor (Supplementary Fig. 13d,e). Surprisingly, alanine substitution at Y50A and K190A in dnTRP_R5- Δ His-residues initially designed to interact with the sulfamide moiety of Ru1 via hydrogen bonding-led to only a modest decrease in affinity (that is, ≤ 2.3 -fold increase in K_D), suggesting that hydrophobic interactions may play a more prominent role in cofactor binding than previously anticipated (Supplementary Fig. 10a). The X-ray structure of **Ru1**·R5-ΔHis displays close structural similarity to **Ru1**·RO-ΔHis, with a backbone ΔHis of 0.6 Å and a Ru atom deviation of 1.0 Å between the two structures (Fig. 4b and

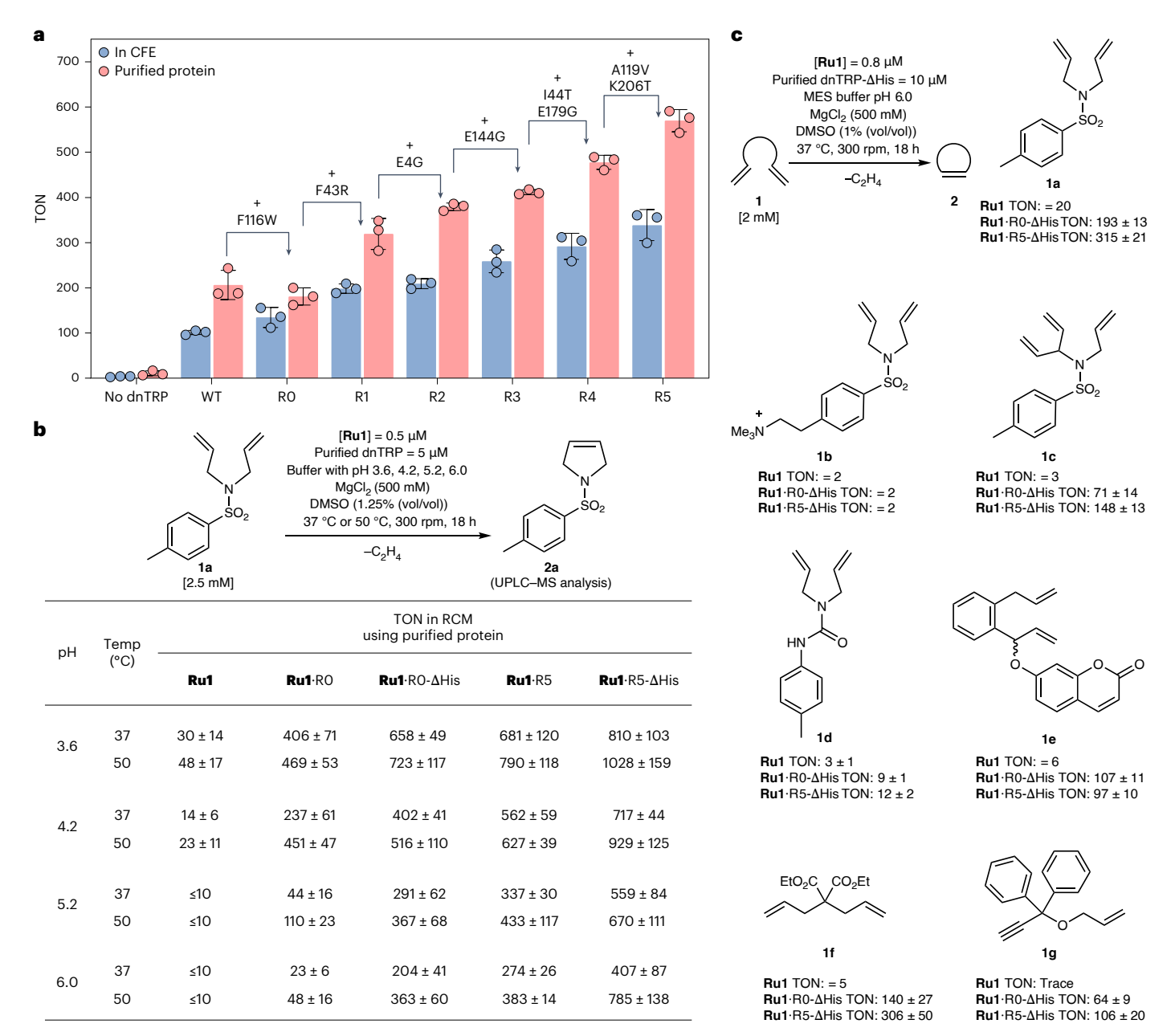


Fig. 3 | **Improving metathase activity of Ru1·dnTRP by directed evolution. a**, A summary of the TON (at pH 4.2, 18 h) of selected **Ru1·dnTRPs** along the evolutionary trajectory, using CFE (blue bars) or purified samples (salmon bars). The beneficial mutations identified during each evolutionary round are highlighted with an arrow. The data for TONs are presented as mean values of three replicates (n = 3), with the error bars representing standard deviation. For the CFE assay, biological replicates were performed. For purified proteins, replicates were independently performed using the same stock of purified dnTRPs. **b**, The effect of pH and temperature (Temp) on the TON for RCM of

substrate ${f 1a}$ using purified dnTRP and dnTRP- Δ His proteins (the N-terminal hexa-histidine and TEV cleavage sequence were removed proteolytically) (Supplementary Fig. 9). ${f c}$, Substrate scope of purified ${f Ru1}$ -dnTRP- Δ His. The data in ${f b}$ and ${f c}$ are displayed as mean values \pm standard deviation of three replicates (n=3). The replicates were independently performed using the same stock of purified dnTRPs. WT, wild type. The details regarding the RCM conditions, sample processing and product quantification are summarized in the Methods, Supplementary Methods and Supplementary Fig. 12.

Supplementary Fig. 13f). Notably, compared with $\mathbf{Ru1}\cdot \mathbf{RO} \cdot \Delta \mathbf{His}$, the evolved variant $\mathbf{Ru1}\cdot \mathbf{R5} \cdot \Delta \mathbf{His}$ features an expanded and less hydrophilic channel leading to the active site, which results from the three critical E4G, E144G and E179G mutations (Fig. 4c and Supplementary Fig. 13g,h). These probably contribute to the increased affinity of dnTRP_R5- $\Delta \mathbf{His}$ (versus dnTRP_R0- $\Delta \mathbf{His}$; Supplementary Fig. 9c) and hinder the approach of hydrophilic species (including GSH, OH $^-$ and so on) that lead to cofactor inhibition.

In developing a computational model of **Ru1**·R5-ΔHis, the structure was predicted using AlphaFold2 and further refined using

Rosetta FastRelax in the presence of **Ru1**. Yet, the resulting models did not accurately reflect the deeper placement of the **Ru1** cofactor as observed in the crystal structure. Attempts to correct the ligand placement with both physics-based Rosetta GALigandDock⁶¹ and deep-learning-based tools like AlphaFold3 (ref. 62), Chai-1 (ref. 63), Boltz-1 (ref. 64) and PLACER⁶⁵ were relatively unsuccessful, with the deep-learning-based methods notably struggling with predicting the precise geometry of **Ru1** possibly due to lack of training examples with similar structures (Supplementary Fig. 14d,e). Chai-1 (ref. 63) showed improved placement of **Ru1** in the expected orientation,

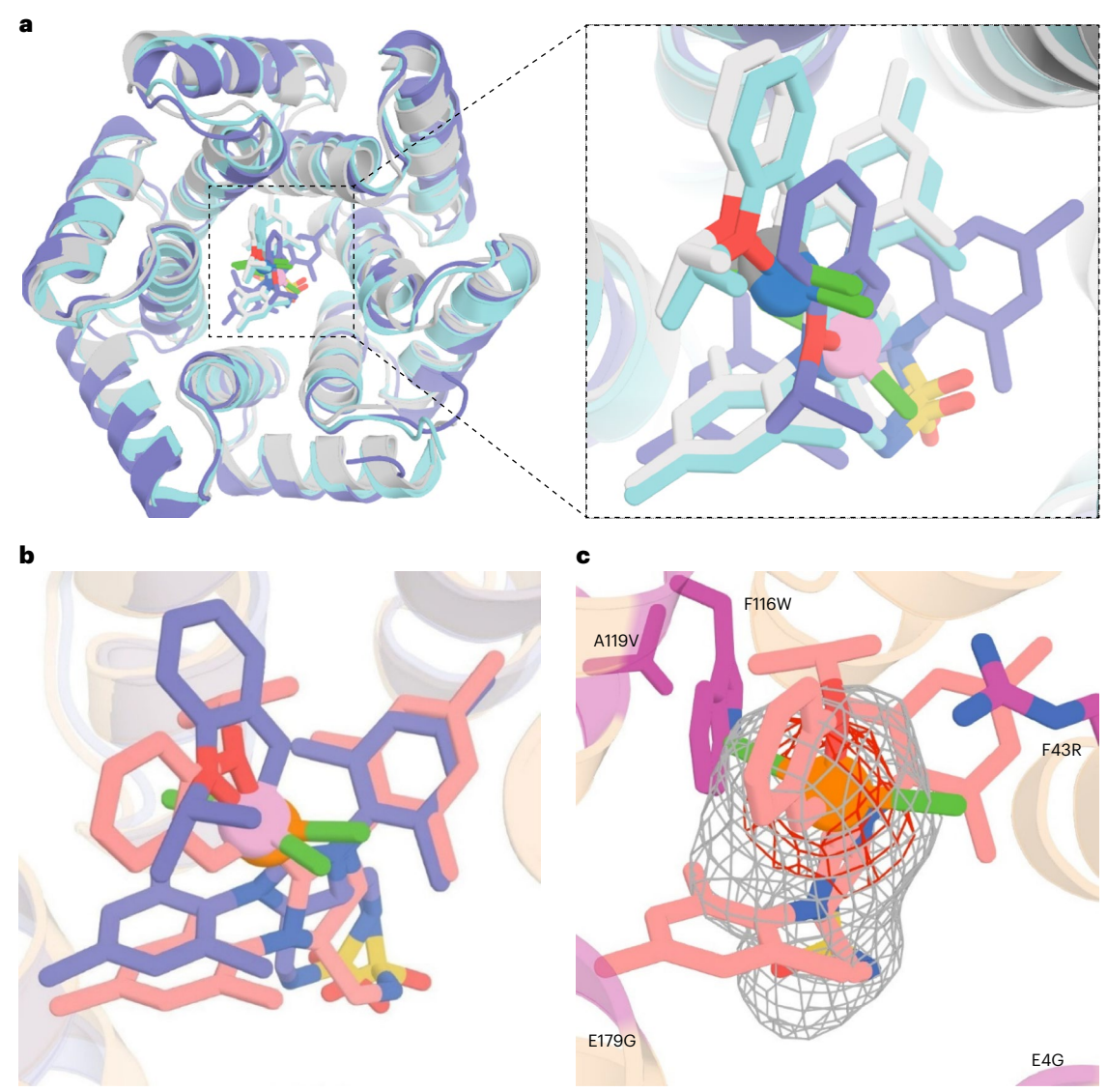


Fig. 4 | Structural analysis of Ru1-dnTRPs. a, An overlay of the design models of Ru1-dnTRP_18 (grey, ruthenium: dark grey sphere), Ru1-R0- Δ His (cyan, ruthenium: blue sphere) and the X-ray structure of Ru1-R0- Δ His (purple, ruthenium: pink sphere, PDB: 8S6P). b, Expanded overlay view around the Ru1 cofactor for Ru1-R0- Δ His (purple, ruthenium: pink sphere) and Ru1-R5- Δ His (wheat, ruthenium: orange sphere, PDB: 9H3C). c, Expanded view of the inner

cavity **Ru1**-R5- Δ His. The ruthenium cofactor (colour-coded sticks, Ru: orange sphere) and the mutated residues (magenta) identified in the directed evolution are highlighted. Fo-Fc omit map contoured at 1σ (grey) highlighting the approximate cofactor position, and anomalous electron density map contoured at 1.0σ (red) highlighting the position of the ruthenium. All the protein scaffolds are displayed as a cartoon representation.

and Ru atom within 1 Å of X-ray, albeit still struggling with the exact geometry of **Ru1** (Supplementary Fig. 14a-c). These discrepancies highlight the challenges faced by current computational models in accurately predicting the complex interplay between protein folds and the unique nature of organometallic cofactors, emphasizing the urgent need for improved modelling techniques capable of handling such chemically diverse cofactors.

Whole-cell RCM catalysed by Ru1·dnTRP-∆His

In light of the remarkable improvement in catalytic performance of **Ru1**·R5, we set out to evaluate its RCM activity in the presence of GSH. For this purpose, we spiked purified samples of **Ru1**·R5- Δ His with increasing concentrations of GSH (Supplementary Fig. 11b). In contrast to the free cofactor **Ru1**, the dnTRP- Δ His host protein protects the thiophilic **Ru1** cofactor from poisoning by GSH: at [GSH] = 1.28 mM, **Ru1**·R5- Δ His maintains > 20% of its RCM activity, whereas **Ru1** is completely inactivated at [GSH] \geq 40 μ M. Encouraged by these findings, we tested whether RCM activity could be detected in the

cytoplasm of E. coli. To safeguard E. coli's viability, whole-cell metathesis experiments were performed at pH 6.0. For this purpose, we treated E. coli cells expressing cytoplasmic dnTRP RO and dnTRP R5 with varying concentrations of **Ru1** (that is $1 \le [\text{Ru1}] \le 10 \,\mu\text{M}$). We used cytoplasmic dnTRR instead of dnTRR-ΔHis, as the former exhibited a markedly higher expression level and facilitated its subsequent purification (Supplementary Fig. 15a). Following incubation and thorough washing, the substrate 1a was added to the cell suspension and RCM activity (at pH 6.0) was quantified by ultra-performance liquid chromatography. At [**Ru1**] \leq 2 μ M, the cells expressing cytoplasmic dnTRP_R5 exhibited notably higher yields of product 2a, compared to dnTRP_RO (Supplementary Fig. 15b,c). Cell viability after RCM was evaluated relying on a colony forming assay, confirming the whole-cell compatibility of RCM catalysed by Ru1·R5 (>50 % colonies remaining after whole-cell RCM, Supplementary Fig. 15d). Inductively coupled plasma mass spectrometry (ICP-MS) analysis revealed that both dnTRP-expressing strains accumulated more than 2.5-fold higher Ru levels compared with E. coli harbouring the empty plasmid.

Although the mean Ru concentration in cells expressing dnTRP_R5 $(343.3 \pm 41.6 \text{ ng g}^{-1}\text{ wet cell weight})$ was higher than in those expressing dnTRP_R0 $(286.7 \pm 80.2 \text{ ng g}^{-1})$, the difference was not statistically significant (P > 0.05, unpaired two-tailed t-test, n = 3) (Fig. 5b and Supplementary Fig. 16).

With this activity screen, we set out to further evolve Ru1·R5 for enhanced RCM activity in *E. coli* whole cells (Supplementary Fig. 17a). Guided by the X-ray structure of **Ru1**·R5-ΔHis, we selected four residues (L8, L113, A148 and L183) (Supplementary Fig. 17b) located in the proximity of the ruthenium for randomization with 17 amino acid residues (except Cvs and Pro). The activity of these 68 variants was evaluated using E. coli whole cells for RCM of substrate 1a. All beneficial mutations resulted from the introduction of hydrophobic residues (Supplementary Fig. 17c). The most active variants **Ru1**·R5 A148I and Ru1·R5 L183M were further recombined with hydrophobic residues of Ala, Phe, Gly, Ile, Met and Val at position 183 and Phe, Gly, Ile, Leu, Met and Val at position 148, respectively. The variant Ru1·R5 A148V/ L183M exhibited the highest cytoplasmic RCM activity (2.5- and 10.6-fold versus **Ru1**·R5 and **Ru1**·R0, respectively) (Fig. 5c). Although reduced GSH is a major intracellular inhibitor of precious-metal-based catalysis, it is probably not the only cytoplasmic metabolite that compromises ArM activity. Notably, the evolved artificial metathase exhibited markedly higher activity than its parent in whole-cell experiments, suggesting that directed evolution has minimized the impact of intracellular deactivating factors. This improved biocompatibility enables effective RCM in the cytoplasm of E. coli, as further illustrated by the in situ release of umbelliferone 3e, an RCM reaction with potential utility for intracellular signalling or prodrug activation^{19,46} (Fig. 5c).

Next, the binding affinity and catalytic performance of these evolved variants were investigated using purified dnTRP-ΔHis (Supplementary Fig. 19a,b). Ru1·R5_A148I/L183M-ΔHis and Ru1·R5_ A148V/L183M-ΔHis exhibited comparable binding affinity to Ru1. R5-ΔHis (both at pH 3.6 and 6.0). To validate the biocompatibility, activity profiles of purified **Ru1**·dnTRP variants were evaluated across a range of GSH concentrations $(0.25 \le [GSH] \le 4 \text{ mM}$, corresponding to 250-4,000 equiv. versus **Ru1**), reflecting the physiological concentrations in the cytoplasm^{66,67}. Gratifyingly, all variants exhibited improved TON in the RCM of 1a, with up to a 2.1-fold increase (versus **Ru1**·R5-ΔHis at pH 6.0) (Supplementary Fig. 19c). Interestingly, the purified variant **Ru1**·R5 A148I-ΔHis afforded superior TONs compared with variants **Ru1**·R5 A148I/L183M-ΔHis and **Ru1**·R5 A148V/ L183M-ΔHis in the presence of GSH, despite the fact that the latter two variants exhibited higher yields of product 2a in the cytoplasmic assay. In addition, to highlight the improved shielding ability of the dnTRP variants, we evaluated the RCM performance of purified **Ru1**·dnTRP-ΔHis variants with substrates **1a**, **1e**, **1f** and **1g** in the presence of [GSH] = 1.5 mM. Gratifyingly, these variants afforded markedly higher TONs than with **Ru1**·R5-ΔHis for RCM products **2a**, **3e**, **2f** and **2g** (Fig. 5 and Supplementary Fig. 20). Collectively, these results highlight the adaptation of the evolved artificial metathases to the deleterious effects of thiols in the cytoplasm of E. coli and demonstrate their robustness and feasibility for performing RCM in living systems.

Conclusion

This study presents an example of combining an artificial preciousmetal cofactor $\mathbf{Ru1}$ with a de novo-designed tandem-repeat protein dnTRP. The resulting ArM catalyses ring-closing olefin metathesis, a new-to-nature reaction. The remarkable stability of the dnTRP markedly simplified the directed evolution protocol, enabling the screening of CFEs. By relying on an endpoint assay, this screening protocol led to the identification of an evolved octuple mutant $\mathbf{Ru1}$ -RS exhibiting \geq 12- and 40-fold increase in TON compared with the parent enzyme $\mathbf{Ru1}$ -RO and the free cofactor $\mathbf{Ru1}$, respectively. The evolved variant $\mathbf{Ru1}$ -RS proved active in the cytoplasm of E. coli, thus enabling the

further evolution of metathase activity in whole cells. By achieving over a 5.4-fold increase in TON in E. coli's cytoplasm for the bioorthogonal uncaging of fluorophore 3e, the evolved artificial metathase highlights its potential for in cellulo applications, including real-time bioimaging and targeted prodrug activation. The X-ray crystal structure of both starting and evolved variants revealed discrepancies with the computed design, highlighting the challenges in the computational modelling of protein and organometallic systems simultaneously and suggesting possible avenues for further improvements in docking and prediction algorithms. To complement previously reported de novo ArMs, our system features a Ru1 cofactor anchored exclusively through weak, non-covalent interactions-rather than via dative or covalent bonds with amino acid side chains 52,68,69. This distinctive feature, combined with the modularity of synthetic strong-field ligands coordinated to platinum-group metals, paves the way for expanding the synthetic biology repertoire towards abiotic transformations within whole-cell enzyme cascades. Collectively, these findings represent a major leap in the de novo design and evolution of ArMs for cytoplasmic catalysis. These underscore the potential of integrating computational design and directed evolution for creating and optimizing ArMs, paving the methodology for building in cellulo new-to-nature catalysis beyond natural or repurposed enzymes.

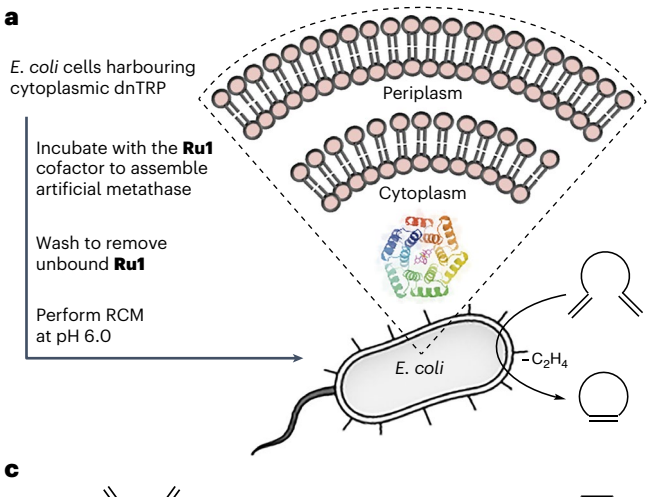
Methods

Generation of mutational libraries of dnTRP

The SSM libraries of dnTRP RO at positions (Q5, E39, F43, E74, L78, L113, E144, A148 and L183) in the first round of screening were generated using dnTRP_18 $_$ F116W (dnTRP $_$ R0) as the template. The SSM libraries for the second round of screening were generated at positions (E4, Q5, E39, E109, E144 and E179) using dnTRP_18_F43R/F116W (dnTRP_R1) as the template. The SSM libraries for the third round of screening were generated at positions (Q5, E39, E144 and E179) using dnTRP_18_E4G/ F43R/F116W (dnTRP_R2) as the template (Supplementary Fig. 8b). The primers used for PCRs are listed in Supplementary Table 2. The PCR products were digested with DpnI (37 °C, 20 h), cleaned and intramolecularly cyclized using the Golden Gate assembly or Gibson assembly kit. The cyclized products were individually transformed into *E. coli* Top10 Chemically Competent Cells, plated on lysogeny broth (LB) agar plate (supplemented with 50 µg ml⁻¹kanamycin) and cultivated (37 °C, 20 h). The colonies from each library were pooled and the plasmids of the colonies were isolated by miniprep. The resulting plasmids were then individually transformed into *E. coli* LEMO21 chemically competent cells.

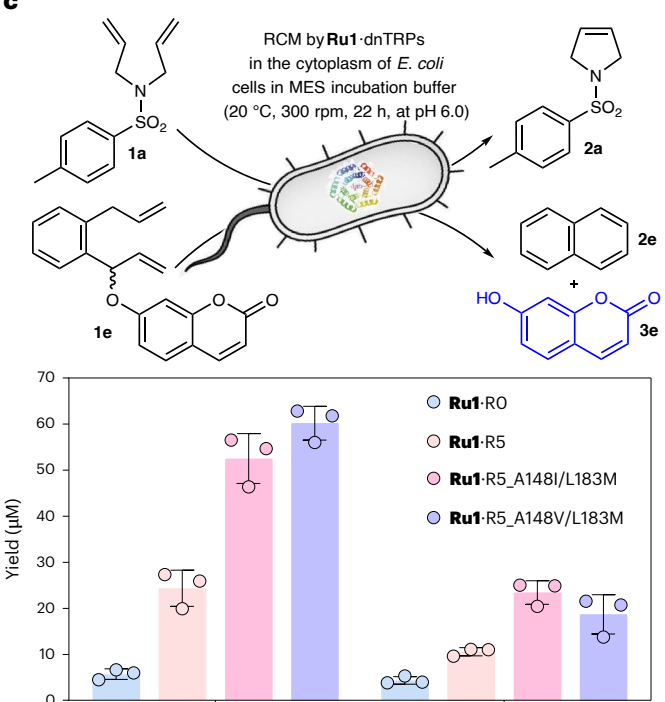
The epPCR library was generated using the dnTRP_R3 (dnTRP_18_E4G/F43R/F116W/E144G) as a template. In brief, epPCR was conducted using Taq polymerase 2X Master Mix supplemented with varying concentrations (from 0.1 to 0.5 mM) of MnCl₂. The PCR products were digested with Dpnl (37 °C, 16 h), cleaned and assembled into the pET-29b vector using the Golden Gate assembly kit. The assembled products were transformed into *E. coli* Top10 Chemically Competent Cells, plated on LB agar plates (supplemented with 50 μg ml $^{-1}$ kanamycin) and cultivated (37 °C, 20 h). Mutational frequencies were assessed by sequencing 16 random colonies from each MnCl₂ concentration, and the results are summarized in Supplementary Fig. 8f. The selected library with a mutational frequency of 4.1 (at 0.15 mM MnCl₂) underwent further processing and transformation into *E. coli* LEMO21.

The fragment shuffling library was generated using Gibson Assembly. In brief, the DNA sequence of dnTRP was separated into five fragments (with sequence lengths varying from 160 to 190 bp) and individually amplified (Supplementary Table 3). Plasmids of selected variants from rounds 3 and 4 were used as the templates for the PCR amplification of the fragments (Supplementary Fig. 8). After DpnI digestion (37 °C, 16 h) and cleanup, the fragments were assembled with the pET-29b vector backbone using the Gibson assembly. The assembled products were transformed into *E. coli* DH5a electro-competent cells, plated on LB agar plates



Strain	Cell fragment	Ruthenium (ng g ⁻¹ in cell wet weight)
Empty vector	Soluble	116.7 ± 11.5
dnTRP_RO	Soluble	286.7 ± 80.2
dnTRP_R5	Soluble	343.3 ± 41.6

b



Variant (purified)	Product	TON (pH 6.0)	TON (with 1.5 × 10 ³ equiv. GSH, pH 6.0
	2a	322 ± 15	78 ± 15
Dod DE ALE	3e	69 ± 11	13 ± 1
Ru1·R5-∆His	2f	379 ± 12	49 ± 3
	2 g	102 ± 20	39 ± 12
	2a	398 ± 29	116 ± 10
Ru1 ·R5_A148I/	3e	63 ± 21	21 ± 2
L183M-ΔHis	2f	447 ± 80	96 ± 19
	2 g	125 ± 33	69 ± 22
	2 a	380 ± 53	117 ± 6
Ru1 ·R5_A148V/ L183M-ΔHis	3e	36 ± 5	18 ± 1
	2f	272 ± 22	79 ± 14
	2 g	121 ± 44	77 ± 27

Fig. 5 | **RCM in the cytoplasm of** *E. coli.* **a**, A schematic representation of the protocol applied for *E. coli* whole-cell RCM by **Ru1**·dnTRPs. **b**, Ruthenium content in the soluble fragment of *E. coli*, determined by ICP-MS. **c**, RCM of substrates **1a** and **1e** by the evolved variants **Ru1**·R5_A148I/L183M and **Ru1**·R5_A148I/L183M in the cytoplasm of *E. coli*. For the RCM of **1e**, the TON was determined by quantifying the product **3e** (by fluorescence) (Supplementary Fig. 18). The results represent the mean of three biological replicates with the error bars indicating standard deviations (*n* = 3). MES incubation buffer: 50 mM, MgCl₂ (100 mM),

glycerol (5% (vol/vol)), 0.02% (wt/vol) poloxamer 188, pH 6.0. **d**, A summary of the TONs obtained for the evolved **Ru1**-dnTRP- Δ His variants, using purified samples for the RCM of substrates **1a**, **1e**, **1f** and **1g** (yielding the products **2a**, **3e**, **2f** and **2g**, respectively), both in the absence and the presence of glutathione (GSH). The data in **d** are displayed as mean values \pm standard deviations of three replicates (n = 3). The replicates were independently performed using the same stock of the purified dnTRP- Δ His proteins.

(supplemented with 50 μg ml $^{-1}$ kanamycin) and cultivated (37 °C, 20 h). The colonies were pooled and their plasmid DNA was extracted, followed by transformation into *E. coli* LEMO21. The colonies were inoculated in the culture (1 ml, ZYP auto-induction medium) in the 96-well plate to express dnTRP, as described in the Supplementary Methods.

Development of the high-throughput screening assay in the 96-well plate

The stock solution of **Ru1** for RCM with the substrate **1a** in the screening assay was prepared as follows. A stock solution of **Ru1** (1 mM in dimethyl sulfoxide (DMSO)) was first prepared. An aliquot (10 μ l) of this solution was transferred into a glass vial (2 ml, clear robo vial, 9 mm thread, item

no. VT009-1232) and chilled onice (1 min). The ice-chilled NaOAc buffer (990 μ l, 100 mM, MgCl₂ (500 mM), pH 4.2) was then added to the vial and gently mixed on ice. The resulting **Ru1** solution ([**Ru1**] = 10 μ M) was used for the RCM reaction.

The freshly prepared CFE (95 μ l, Supplementary Methods) of the libraries was transferred into a new assay plate (MASTERBLOCK, 96 well, polypropylene (PP), 0.5 ml, V-bottom) using the Liquidator 96-channel benchtop pipette (volume range of 5–200 μ l). After chilling the plate on ice for 15 min, the **Ru1** cofactor (5 μ l, 10 μ M stock in NaOAc buffer (100 mM, MgCl $_2$ (500 mM), pH 4.2)) was added in the wells using a multichannel pipette. The plate was then covered with a thick aluminium sealing film (AlumaSeal 96 film) and incubated (30 °C,

250 rpm, 2 h). Then, the aluminium film was lifted and the substrate $1a\,(1\,\mu l,250\,\mu M\,\text{stock}$ in DMSO, final concentration 2.5 mM) was added using multichannel pipette. The plate was resealed and incubated $(37\,^\circ\text{C},300\,\text{rpm},18\,\text{h})$ for the RCM reaction. After incubation, the plate was chilled $(10\,\text{min}$ on ice) and methanol was added $(400\,\mu l,\text{supplemented}$ with benzyltriethyl-ammonium bromide $(200\,\mu M)$ as internal standard). The plate was resealed and incubated $(37\,^\circ\text{C},300\,\text{rpm},30\,\text{min})$ to quench the reaction. The plate was centrifuged $(4\,^\circ\text{C},4,400g,30\,\text{min})$ and the clear supernatant $(350\,\mu l)$ was transferred to a new analysis plate (MASTERBLOCK, 96 well, PP, 0.5 ml, V-bottom) and subjected to ultra performance liquid chromatographymass spectrometry (UPLC–MS) analysis. The schematic presentation of the screening protocol, the step-to-step rounds of evolutionary campaigns and the identified variants from each round are displayed in Supplementary Fig. 8.

RCM of different olefin substrates using purified Ru1·dnTRPs

RCM of substrates 1b, 1c, 1d, 1e, 1f and 1g to afford the corresponding cyclized products 2b, 2c, 2d, 2e, 2f, 2g and 3e-corresponding to the product cogenerated with 2e in RCM of 1e-was performed using a modified protocol that was used for cyclized product 2a. In brief, **Ru1** (5 µl from a freshly prepared stock (16 µM in ice-chilled 2-morpholinoethanesulfonic acid (MES) buffer (100 mM, MgCl₂ (500 mM), pH 6.0, final concentration is 0.8 μ M))) was added to the dnTRP_RO/R5-ΔHis protein sample (95 μl, MES buffer (100 mM, MgCl₂ (500 mM), purified dnTRP RO/R5- Δ His (10.5 μ M), pH 6.0)) in a glass vial (2 ml, clear robo vial, 9 mm thread, item no. VT009-1232). The vials were tightly sealed and incubated (30 °C, 250 rpm, 2 h). After chilling (5 min, on ice), the substrate 1b, 1c, 1d, 1e, 1f or 1g (1 μ l, 200 mM stock in DMSO, [substrate] $_{\text{final}}$ = 2.0 mM) was added. The vials were resealed and incubated (37 °C, 300 rpm, 18 h). To prepare samples for UPLC-MS analysis in the RCM reactions of 1a, 1b, 1c and 1d, methanol (900 μ l, containing benzyltriethyl-ammonium bromide (200 μ M) as the internal standard) was added. To prepare samples for gas chromatography-mass spectrometry analysis, EtOAc (500 μl, containing 1 mM biphenyl as the internal standard) was added to RCM samples of 1e, EtOAc (500 μ l, supplemented with [naphthalene] = 1 mM) as the internal standard) for RCM samples of 1f and 1g. After adding methanol or EtOAc, all vials were sealed, incubated (37 °C, 300 rpm, 30 min) and centrifuged (4 °C, 4,400g, 30 min). The clear supernatant (800 µl:

RCM of 1a. 1b. 1c and 1d) was subjected to UPLC-MS analysis. The

upper EtOAc phase (300 µl: RCM of 1e, 1f and 1g) was subjected to gas

chromatography-mass spectrometry analysis. Calibration curves for

determining the yield/TON of cyclized products 2a, 2b, 2c, 2d, 2e, 3e,

In cellulo RCM by Ru1·dnTRPs

2f or 2g are displayed in Supplementary Fig. 12.

To assemble the cytoplasmic **Ru1**·dnTRPs (cells harbouring an empty vector were used as negative control), freshly collected cells were gently resuspended in MES working buffer (50 mM, MgCl₂ (100 mM), glycerol (5% (vol/vol)), pH 6.0) to a cell density around 25 g l^{-1} (wet cell weight). The cell samples (1 ml) were individually transferred into a round-bottom 24-well plate, supplemented with the cofactor Ru1 (1, 2, 5 or 10 μl from a freshly prepared stock (1 mM in DMSO)) and incubated (15 °C, 800 rpm, 1 h) for in cellulo assembly of artificial metathase. After incubation, cells were isolated by centrifugation (4 °C, 2,600g, 3 min). The resulting cells were then subjected to five washing cycles, which involved cell resuspension in MES working buffer (1 ml), incubation (15 °C, 1,000 rpm, 15 min) and cell collection by centrifugation (20 °C, 2,600g, 3 min). The cells then were resuspended in MES working buffer (0.33 ml) at a cell density around 75 g l^{-1} (wet cell weight). The resuspended cell sample (100 µl) was aliquoted into a 96-well plate (MASTERBLOCK, 96 well, PP, 0.5 ml, V-bottom), supplemented with substrate 1a (2.5 mM, 1 µl from a stock (250 mM in DMSO and incubated (20 °C, 300 rpm, 22 h) under sealed conditions.

The subsequent steps concerning reaction quenching, sample preparation and UPLC-MS analysis were carried out as the protocol described in the Supplementary Methods. The results are summarized in Supplementary Fig. 15b.

Engineering of dnTRP R5 in cytoplasm of E. coli

The plasmid of pET-29b dnTRP_R5 was used as template for constructing of dnTRP R5 L8X, L113X, A148X and L183X (where X represents any amino acid except cysteine and proline). The PCR amplifications were conducted in a 96-well PCR plate using the corresponding primers, Supplementary Table 4. The PCR products were first digested with DpnI (37 °C, 20 h) and then individually transformed (3 μl) into E. coli Top10 Chemically Competent Cells (15 µl) in a new 96-well PCR plate. The transformed cells were individually plated on LB agar (supplemented with 50 µg ml⁻¹ kanamycin) and cultivated (37 °C, 20 h). The colonies with the correct sequence were cultivated in LB medium (3 ml, supplemented with 50 µg ml⁻¹ kanamycin), and the plasmids were isolated by miniprep. The plasmids were then individually transformed into E. coli LEMO21 chemically competent cells in a 96-well PCR plate. The transformed cells were plated on LB agar plate (with 50 μg ml⁻¹ kanamycin) and incubated (37 °C, 14 h). The colonies were picked and inoculated into a main culture (ZYP auto-induction medium (30 ml), kanamycin (400 μg ml⁻¹), in a 250 ml baffled shaking flask) to express the corresponding TRPs. The culture was initially incubated $(37 \, ^{\circ}\text{C}, 180 \, \text{rpm})$ to an $OD_{600} = 0.3 - 0.4$, followed by further incubation $(20 \, ^{\circ}\text{C}, 180 \, \text{rpm}, \ge 18 \, \text{h})$ to an $OD_{600} \ge 14$. After expression, the cells were collected by centrifugation (4 °C, 2,600g, 10 min).

To perform screening of the 68 dnTRP R5 variant library at positions L8, L113, A148 and L183 for cytoplasmic RCM, a simplified protocol was applied. In brief, the collected cells were immediately resuspended in the MES incubation buffer (50 mM, MgCl₂ (100 mM), glycerol (5% (vol/vol)), 0.02% (wt/vol) poloxamer 188, pH 6.0) to a cell density at 25 g l⁻¹ (wet cell weight). The cell samples (0.3 ml) were transferred into a 96-well plate (MASTERBLOCK, 96 well, PP, 0.5 ml, V-bottom), supplemented with the cofactor **Ru1** (0.5 µl from a freshly prepared stock (0.9 mM in DMSO), final concentration 1.5 µM) and incubated (30 °C, 1,000 rpm, 1.5 h). After incubation, the cells were obtained by centrifugation (25 °C, 2,600g, 5 min). The obtained cell samples were then subjected to two consecutive washing step, which consisted of cell resuspension in MES washing buffer (0.3 ml, 50 mM, MgCl₂(100 mM), glycerol (5% (vol/vol)), 0.02% (wt/vol) poloxamer 188. 0.0075% (vol/vol) Triton X-100, pH 6.0), incubation (30 °C, 1,000 rpm, 30 min) and cell collection by centrifugation (25 °C, 2,600g, 3 min). The cells were then resuspended in the MES incubation buffer at a cell density around 75 g (wet cell weight) per litre. To perform the whole-cell RCM at pH 4.2 or 5.2, cells were resuspended in NaOAc incubation buffer (0.1 ml, 50 mM, MgCl₂ (100 mM), glycerol (5% (vol/vol)), 0.02% (wt/vol) poloxamer 188) with pH at 4.2 or 5.2. The subsequent steps of cytoplasmic RCM (1a) were conducted as described above the 'In cellulo RCM by Ru1·dnTRPs' section. A schematic representation of the screening protocol for the directed evolution of Rul·dnTRP in the cytoplasm of E. coli is presented Supplementary Fig. 17.

For the cytoplasmic RCM using substrate $\bf 1e$, the resuspended cell sample (100 µl) was transferred into a 96-well plate (Nunc Micro-Well, Nunclon Delta-Treated, flat bottom), supplemented with substrate $\bf 1e$ (1 mM, 1 µl of a 100 mM stock in DMSO)), sealed with a transparent polystyrene lid and subjected to continuous fluorescence recording (excitation: 325 nm, emission: 450 nm, room temperature, Tecan Infinite M1000 PRO). The calibration curve for fluorogenic quantification was generated by supplementing and recording the fluorescence of a gradient of concentrations (5–80 µM) of the fluorescent product $\bf 3e$ (Supplementary Fig. 12a) in MES buffer (100 mM, MgCl2 (500 mM), pH 6.0) or $\bf \it E. coli$ cell suspensions ($\bf \it E. coli$ cells harbour empty vector, 75 g $\bf l^{-1}$ wet cell weight, in MES incubation buffer) (Supplementary Fig. 18b,e).

ICP-MS

Freshly collected cells expressing dnTRP RO and dnTRP R5 (cells harbouring an empty vector were used as controls) were immediately resuspended in MES working buffer (50 mM, MgCl₂ (100 mM), glycerol (5% (vol/vol)), pH 6.0) at a cell density of 25 g l⁻¹ (wet cell weight). The resuspended cell samples (20 ml) were transferred into a Falcon tube (50 ml, polypropylene Conical Tube, 30 mm × 115 mm style) and supplemented with the cofactor **Ru1** (40 µl from a freshly prepared stock (1 mM in DMSO), final concentration is 2 µM). The samples were incubated (20 °C, 300 rpm, 1 h), after which the cells were collected by centrifugation (4 °C, 2,600g, 10 min). The resulting cells were then subjected to five washing step cycles, which involved cell resuspension in MES working buffer (20 ml), incubation (20 °C, 300 rpm, 15 min) and cell collection by centrifugation (4 °C, 2.600g. 8 min). The cells were then frozen (-20 °C, 22 h), thawed (37 °C, 300 rpm, 30 min) and resuspended in a modified MES working buffer (5 ml, 50 mM, MgCl₂ (500 mM), glycerol (5% (vol/vol)), pH 6.0) for cell fragmentation. A schematic representation of the steps for the preparation of cell fragments is summarized in Supplementary Fig. 16a. In brief, the cells were lysed on ice by sonication (1 s on-off, 60% amplitude, 5 min). The clear supernatant A (hereafter refers to as clear supernatant obtained by cell lysis of sonication) and cell pellet A (referred to as cell debris) were obtained by centrifugation (4 °C, 12,000g, 10 min). The clear supernatant A was further processed with an ultracentrifugation (4 °C, 87,000g, 2.5 h) to afford the clear supernatant B (hereafter referred to cytoplasmic fragment) and cell pellet B (hereafter referred to membranous fragments). Cell pellet A and cell pellet B were fully resuspended in MES working buffer (5 ml). The contents of dnTRP R5 in the prepared fragments were analysed by SDS-polyacrylamide gel electrophoresis, Supplementary Fig. 16b. For ICP-MS, the samples of clear supernatant B from three independently performed experiments were pooled, aliquoted and subjected to ICP-MS analysis.

Reporting summary

Further information on research design is available in the Nature Portfolio Reporting Summary linked to this article.

Data availability

The original materials, methods and data underlying the findings of this study are available within the Article and its Supplementary Information. The PDB accession codes of apo dnTRP_RO- Δ His, **Ru1**·RO- Δ His and **Ru1**·R5- Δ His are 9GVF, 8S6P and 9H3C, respectively. All other data are available from the authors upon request. Source data are provided with this paper.

Code availability

The source code for the de novo scaffold design is available via GitHub at https://github.com/ikalvet/denovo metathase design.

References

- Hanefeld, U., Hollmann, F. & Paul, C. E. Biocatalysis making waves in organic chemistry. Chem. Soc. Rev. 51, 594–627 (2022).
- Buller, R. et al. From nature to industry: harnessing enzymes for biocatalysis. Science 382, eadh8615 (2023).
- Key, H. M. et al. Beyond iron: iridium-containing P450 enzymes for selective cyclopropanations of structurally diverse alkenes. ACS Cent. Sci. 3, 302–308 (2017).
- 4. Oohora, K., Onoda, A. & Hayashi, T. Hemoproteins reconstituted with artificial metal complexes as biohybrid catalysts. *Acc. Chem. Res.* **52**, 945–954 (2019).
- Mirts, E. N., Bhagi-Damodaran, A. & Lu, Y. Understanding and modulating metalloenzymes with unnatural amino acids, non-native metal ions, and non-native metallocofactors. Acc. Chem. Res. 52, 935–944 (2019).

- Kim, J. K. et al. Elucidating the role of metal ions in carbonic anhydrase catalysis. *Nat. Commun.* 11, 4557 (2020).
- Shima, S. et al. Reconstitution of [Fe]-hydrogenase using model complexes. Nat. Chem. 7, 995–1002 (2015).
- Sauer, D. F. et al. A highly active biohybrid catalyst for olefin metathesis in water: impact of a hydrophobic cavity in a β-barrel protein. ACS Catal. 5, 7519–7522 (2015).
- Philippart, F. et al. A hybrid ring-opening metathesis polymerization catalyst based on an engineered variant of the β-barrel protein FhuA. Chem. Eur. J. 19, 13865–13871 (2013).
- Srivastava, P., Yang, H., Ellis-Guardiola, K. & Lewis, J. C. Engineering a dirhodium artificial metalloenzyme for selective olefin cyclopropanation. *Nat. Commun.* 6, 7789 (2015).
- Yang, H., Srivastava, P., Zhang, C. & Lewis, J. C. A general method for artificial metalloenzyme formation through strain-promoted azide-alkyne cycloaddition. *ChemBioChem* 15, 223–227 (2014).
- Bos, J., Fusetti, F., Driessen, A. J. M. & Roelfes, G. Enantioselective artificial metalloenzymes by creation of a novel active site at the protein dimer interface. *Angew. Chem. Int. Ed.* 51, 7472–7475 (2012).
- Podtetenieff, J., Taglieber, A., Bill, E., Reijerse, E. J. & Reetz, M. T. An artificial metalloenzyme: creation of a designed copper binding site in a thermostable protein. *Angew. Chem. Int. Ed.* 49, 5151–5155 (2010).
- Reig, A. J. et al. Alteration of the oxygen-dependent reactivity of de novo Due Ferri proteins. *Nat. Chem.* 4, 900–906 (2012); erratum 4, 1050 (2012).
- Basler, S. et al. Efficient Lewis acid catalysis of an abiological reaction in a de novo protein scaffold. Nat. Chem. 13, 231–235 (2021).
- Dydio, P. et al. An artificial metalloenzyme with the kinetics of native enzymes. Science 354, 102–106 (2016).
- Bos, J., Browne, W. R., Driessen, A. J. M. & Roelfes, G. Supramolecular assembly of artificial metalloenzymes based on the dimeric protein lmrr as promiscuous scaffold. *J. Am. Chem.* Soc. 137, 9796–9799 (2015).
- Wilson, M. E. & Whitesides, G. M. Conversion of a protein to a homogeneous asymmetric hydrogenation catalyst by site-specific modification with a diphosphinerhodium(I) moiety. J. Am. Chem. Soc. 100, 306–307 (1978).
- Eda, S. et al. Biocompatibility and therapeutic potential of glycosylated albumin artificial metalloenzymes. *Nat. Catal.* 2, 780–792 (2019).
- 20. Vornholt, T. et al. Systematic engineering of artificial metalloenzymes for new-to-nature reactions. *Sci. Adv.* **7**, eabe4208 (2021).
- 21. Filice, M. et al. Preparation of an immobilized lipase-palladium artificial metalloenzyme as catalyst in the heck reaction: role of the solid phase. *Adv. Synth. Catal.* **357**, 2687–2696 (2015).
- Lopez, S., Marchi-Delapierre, C., Cavazza, C. & Ménage, S. A selective sulfide oxidation catalyzed by heterogeneous artificial metalloenzymes iron@NikA. Chem. Eur. J. 26, 16633–16638 (2020).
- Martins, F. L., Pordea, A. & Jäger, C. M. Computationally driven design of an artificial metalloenzyme using supramolecular anchoring strategies of iridium complexes to alcohol dehydrogenase. *Faraday Discuss.* 234, 315–335 (2022).
- Garcia-Sanz, C., de las Rivas, B. & Palomo, J. M. Design of a gold nanoparticles site in an engineered lipase: an artificial metalloenzyme with enantioselective reductase-like activity. Nanoscale 16, 6999–7010 (2024).
- Roelfes, G. LmrR: a privileged scaffold for artificial metalloenzymes. Acc. Chem. Res. 52, 545–556 (2019).
- Kato, S., Onoda, A., Schwaneberg, U. & Hayashi, T. Evolutionary engineering of a Cp*Rh(III) complex-linked artificial metalloenzyme with a chimeric beta-barrel protein scaffold. *J. Am. Chem.* Soc. 145, 8285–8290 (2023).

- Blanco, C. O. & Fogg, D. E. Water-accelerated decomposition of olefin metathesis catalysts. ACS Catal. 13, 1097–1102 (2023).
- Sasmal, P. K., Streu, C. N. & Meggers, E. Metal complex catalysis in living biological systems. *Chem. Commun.* 49, 1581–1587 (2013).
- Streu, C. & Meggers, E. Ruthenium-induced allylcarbamate cleavage in living cells. *Angew. Chem. Int. Ed.* 45, 5645–5648 (2006).
- Wittwer, M. et al. Engineering and emerging applications of artificial metalloenzymes with whole cells. Nat. Catal. 4, 814–827 (2021).
- Chordia, S., Narasimhan, S., Paioni, A. L., Baldus, M. & Roelfes, G. In vivo assembly of artificial metalloenzymes and application in whole-cell biocatalysis. *Angew. Chem. Int. Ed.* 60, 5913–5920 (2021).
- Huang, J. et al. Unnatural biosynthesis by an engineered microorganism with heterologously expressed natural enzymes and an artificial metalloenzyme. Nat. Chem. 13, 1186–1191 (2021).
- 33. Gu, Y., Bloomer, B., Liu, Z. N., Clark, D. & Hartwig, J. F. Directed evolution of artificial metalloenzymes in whole cells. *Angew. Chem. Int. Ed.* **61**, e202110519 (2022).
- Liu, Z. N. et al. Assembly and evolution of artificial metalloenzymes within nissle 1917 for enantioselective and site-selective functionalization of C-H and C=C Bonds. J. Am. Chem. Soc. 144, 883–890 (2022).
- 35. Zhao, J. M. et al. Genetic engineering of an artificial metalloenzyme for transfer hydrogenation of a self-immolative substrate in *E. coli's* periplasm. *J. Am. Chem.* Soc. **140**, 13171–13175 (2018).
- Stein, A. et al. A dual anchoring strategy for the directed evolution of improved artificial transfer hydrogenases based on carbonic anhydrase. ACS Cent. Sci. 7, 1874–1884 (2021).
- 37. Jeschek, M. et al. Directed evolution of artificial metalloenzymes for in vivo metathesis. *Nature* **537**, 661–665 (2016).
- Heinisch, T. et al. surface display of streptavidin for directed evolution of an allylic deallylase. Chem. Sci. 9, 5383–5388 (2018).
- Grimm, A. R. et al. A whole cell display platform for artificial metalloenzymes: poly(phenylacetylene) production with a rhodium-nitrobindin metalloprotein. ACS Catal. 8, 2611–2614 (2018).
- Ogba, O. M., Warner, N. C., O'Leary, D. J. & Grubbs, R. H. Recent advances in ruthenium-based olefin metathesis. *Chem. Soc. Rev.* 47, 4510–4544 (2018).
- Kim, Y. W., Grossmann, T. N. & Verdine, G. L. Synthesis of all-hydrocarbon stapled α-helical peptides by ring-closing olefin metathesis. *Nat. Protoc.* 6, 761–771 (2011).
- Blanco, C. O., Cormier, S. K., Koller, A. J., Boros, E. & Fogg, D. E. Olefin metathesis in water: speciation of a leading water-soluble catalyst pinpoints challenges and opportunities for chemical biology. J. Am. Chem. Soc. 147, 9441–9448 (2025).
- 43. Nasibullin, I. et al. Catalytic olefin metathesis in blood. *Chem. Sci.* **14**, 11033–11039 (2023).
- Schunck, N. S. & Mecking, S. In vivo olefin metathesis in microalgae upgrades lipids to building blocks for polymers and chemicals. *Angew. Chem. Int. Ed.* 61, e202211285 (2022).
- Wu, T. et al. Artificial metalloenzyme assembly in cellular compartments for enhanced catalysis. *Nat. Chem. Biol.* 21, 779–789 (2025).
- Sabatino, V., Rebelein, J. G. & Ward, T. R. 'Close-to-Release': spontaneous bioorthogonal uncaging resulting from ring-closing metathesis. J. Am. Chem. Soc. 141, 17048–17052 (2019).
- 47. Zou, Z. et al. Combining an artificial metathase with a fatty acid decarboxylase in a whole cell for cycloalkene synthesis. *Nat. Synth.* **3**, 1113–1123 (2024).
- 48. An, L. N. et al. Hallucination of closed repeat proteins containing central pockets. *Nat. Struct. Mol. Biol.* **30**, 1755–1760 (2023).

- Siegel, J. B. et al. Computational design of an enzyme catalyst for a stereoselective bimolecular diels-alder reaction. *Science* 329, 309–313 (2010).
- 50. Dou, J. Y. et al. De novo design of a fluorescence-activating β-barrel. *Nature* **561**, 485–491 (2018).
- 51. Yeh, A. H. et al. De novo design of luciferases using deep learning. *Nature* **614**, 774–780 (2023).
- 52. Kalvet, I. et al. Design of heme enzymes with a tunable substrate binding pocket adjacent to an open metal coordination site. *J. Am. Chem.* Soc. **145**, 14307–14315 (2023).
- 53. Polizzi, N. F. & DeGrado, W. F. A defined structural unit enables de novo design of small-molecule-binding proteins. *Science* **369**, 1227–1233 (2020).
- 54. Maguire, J. B. et al. Perturbing the energy landscape for improved packing during computational protein design. *Proteins* **89**, 436–449 (2021).
- 55. Doyle, L. et al. Rational design of alpha-helical tandem repeat proteins with closed architectures. *Nature* **528**, 585–588 (2015).
- Arnold, F. H. Innovation by evolution: bringing new chemistry to life (Nobel lecture). *Angew. Chem. Int. Ed.* 58, 14420–14426 (2019).
- Markel, U., Sauer, D. F., Schiffels, J., Okuda, J. & Schwaneberg, U. Towards the evolution of artificial metalloenzymes-a protein engineer's perspective. *Angew. Chem. Int. Ed.* 58, 4454–4464 (2019).
- 58. Wang, Y. J. et al. Directed evolution: methodologies and applications. *Chem. Rev.* **121**, 12384–12444 (2021).
- Lynn, D. M., Mohr, B., Grubbs, R. H., Henling, L. M. & Day, M. W. Water-soluble ruthenium alkylidenes: Synthesis, characterization, and application to olefin metathesis in protic solvents. *J. Am. Chem.* Soc. 122, 6601–6609 (2000).
- 60. Jumper, J. et al. Highly accurate protein structure prediction with AlphaFold. *Nature* **596**, 583–589 (2021).
- Park, H., Zhou, G. F., Baek, M., Baker, D. & DiMaio, F. Force field optimization guided by small molecule crystal lattice data enables consistent sub-angstrom protein-ligand docking. *J. Chem. Theory Comput.* 17, 2000–2010 (2021).
- 62. Abramson, J. et al. Accurate structure prediction of biomolecular interactions with AlphaFold 3. *Nature* **630**, 493–500 (2024).
- Chai Discovery et al. Chai-1: decoding the molecular interactions of life. Preprint at bioRxiv https://doi.org/10.1101/2024.10.10.
 615955 (2024).
- 64. Wohlwend, J. et al. Boltz-1 democratizing biomolecular interaction modeling. Preprint at *bioRxiv* https://doi.org/10.1101/2024.11.19.624167 (2024).
- 65. Seager, S. & Mallén-Ornelas, G. On the unique solution of planet and star parameters from an extrasolar planet transit light curve. *Astrophys. J.* (in the press); preprint at https://doi.org/10.1101/2024.09.25.614868 (2024).
- Fahey, R. C., Brown, W. C., Adams, W. B. & Worsham, M. B. Occurrence of glutathione in bacteria. *J. Bacteriol.* 133, 1126–1129 (1978).
- 67. Schafer, F. Q. & Buettner, G. R. Redox environment of the cell as viewed through the redox state of the glutathione disulfide/glutathione couple. *Free Radic. Biol. Med.* **30**, 1191–1212 (2001).
- 68. Klein, A. S. et al. A de novo metalloenzyme for cerium photoredox catalysis. *J. Am. Chem. Soc.* **146**, 25976–25985 (2024).
- Hou, K. P. et al. De novo design of porphyrin-containing proteins as efficient and stereoselective catalysts. Science 388, 665–670 (2025).

Acknowledgements

T.R.W. thanks the NCCR Molecular Systems Engineering (grant no. 200021_178760) and the Swiss National Science Foundation (grant no. 200020_212088) for funding. We thank R. P. Jakob and T. Maier

from the Biozentrum, University of Basel, for their support and discussions regarding X-ray crystallography studies. We also thank S. Bolotova (Seebeck group, University of Basel) for generously providing the TEV protease. This work was supported by the Open Philanthropy Project Improving Protein Design Fund (to I.K. and D.B.) and Human Frontier Science Program Cross-Disciplinary Fellowship (grant no. LT000838/2018-C to I.K.). We thank L. Goldschmidt and K. VanWormer, respectively, for maintaining the computational and wet lab resources at the Institute for Protein Design.

Author contributions

Conception of the study: T.R.W. and D.B. Computational design and preliminary experimental characterization of dnTRPs: I.K. Synthesis of the **Ru1** cofactor: B.L. Experimental characterization of dnTRPs, optimization of binding affinity optimization, directed evolution and characterization of artificial metathase: Z.Z. Crystallography: K.Z., E.M. and Z.Z. Substrate scope study: D.C., Z.Z., M.L.E., X.Z. and B.L. Native mass spectroscopy: E.M. Supervision throughout the project: T.R.W. and D.B. Wrote the manuscript: Z.Z., I.K., B.L., T.R.W. and D.B. All authors read, contributed to and approved the final version of the manuscript.

Competing interests

The authors declare no competing interests.

Additional information

Supplementary information The online version contains supplementary material available at https://doi.org/10.1038/s41929-025-01436-0.

Correspondence and requests for materials should be addressed to David Baker or Thomas R. Ward.

Peer review information *Nature Catalysis* thanks Gustav Oberdorfer, Jose M. Palomo and the other, anonymous, reviewer(s) for their contribution to the peer review of this work.

Reprints and permissions information is available at www.nature.com/reprints.

Publisher's note Springer Nature remains neutral with regard to jurisdictional claims in published maps and institutional affiliations.

Open Access This article is licensed under a Creative Commons Attribution 4.0 International License, which permits use, sharing, adaptation, distribution and reproduction in any medium or format, as long as you give appropriate credit to the original author(s) and the source, provide a link to the Creative Commons licence, and indicate if changes were made. The images or other third party material in this article are included in the article's Creative Commons licence, unless indicated otherwise in a credit line to the material. If material is not included in the article's Creative Commons licence and your intended use is not permitted by statutory regulation or exceeds the permitted use, you will need to obtain permission directly from the copyright holder. To view a copy of this licence, visit http://creativecommons.org/licenses/by/4.0/.

© The Author(s) 2025

nature portfolio

Corresponding author(s):	Thomas R. Ward
Last updated by author(s):	Sep 2, 2025

Reporting Summary

Nature Portfolio wishes to improve the reproducibility of the work that we publish. This form provides structure for consistency and transparency in reporting. For further information on Nature Portfolio policies, see our <u>Editorial Policies</u> and the <u>Editorial Policy Checklist</u>.

٠.	+~	. +-	ist	
`	_		\sim 1	11 \

For	all st	atistical analyses, confirm that the following items are present in the figure legend, table legend, main text, or Methods section.
n/a	Cor	nfirmed
	\boxtimes	The exact sample size (n) for each experimental group/condition, given as a discrete number and unit of measurement
	X	A statement on whether measurements were taken from distinct samples or whether the same sample was measured repeatedly
\boxtimes		The statistical test(s) used AND whether they are one- or two-sided Only common tests should be described solely by name; describe more complex techniques in the Methods section.
\times		A description of all covariates tested
\times		A description of any assumptions or corrections, such as tests of normality and adjustment for multiple comparisons
	\boxtimes	A full description of the statistical parameters including central tendency (e.g. means) or other basic estimates (e.g. regression coefficient) AND variation (e.g. standard deviation) or associated estimates of uncertainty (e.g. confidence intervals)
\boxtimes		For null hypothesis testing, the test statistic (e.g. <i>F</i> , <i>t</i> , <i>r</i>) with confidence intervals, effect sizes, degrees of freedom and <i>P</i> value noted <i>Give P values as exact values whenever suitable.</i>
\boxtimes		For Bayesian analysis, information on the choice of priors and Markov chain Monte Carlo settings
\times		For hierarchical and complex designs, identification of the appropriate level for tests and full reporting of outcomes
\times		Estimates of effect sizes (e.g. Cohen's d, Pearson's r), indicating how they were calculated
	'	Our web collection an statistics for highesists contains articles on many of the points above

Software and code

Policy information about availability of computer code

Data collection

Experimental data are collected in various softwares of different instruments, including Waters Acquity UPLC system, SHIMADZU GCMS-QP2020, TECAN i-control 2.0, AlphaFold2&3, Gaussian 16, RifGen, and RifDock softwares. The computed atomic coordinates of the ligand used in this study are available in multiple formats on GitHub using this link: https://github.com/ikalvet/denovo_metathase_design.

Data analysis

Experimental data present in the manuscript and supporting information are processed by different softwares, including Microsoft Excel software (2016), OriginLab Origin2019b, GraphPad Prism, and PyMol 2.3.0.

For manuscripts utilizing custom algorithms or software that are central to the research but not yet described in published literature, software must be made available to editors and reviewers. We strongly encourage code deposition in a community repository (e.g. GitHub). See the Nature Portfolio guidelines for submitting code & software for further information.

Data

Policy information about availability of data

All manuscripts must include a data availability statement. This statement should provide the following information, where applicable:

- Accession codes, unique identifiers, or web links for publicly available datasets
- A description of any restrictions on data availability
- For clinical datasets or third party data, please ensure that the statement adheres to our policy

The data that support the findings in this study are available within this article and the Supplementary Information. The PDB accession codes of apo dnTRP_R0- Δ his, Ru1·R0- Δ his, and Ru1·R5- Δ his are 9GVF, 8S6P, and 9H3C, respectively. All other data is available from the authors upon request.

Human research participants

Policy information about studies involving human research participants and Sex and Gender in Research.

Reporting on sex and gender	n/a
Population characteristics	n/a
Recruitment	n/a
Ethics oversight	n/a

Note that full information on the approval of the study protocol must also be provided in the manuscript.

Field-specific reporting

Please select the one below	that is the best fit for your research.	If you	are not sure, read the appropriate sections before making your selection.
X Life sciences	Behavioural & social sciences		Ecological, evolutionary & environmental sciences

For a reference copy of the document with all sections, see <u>nature.com/documents/nr-reporting-summary-flat.pdf</u>

Life sciences study design

All studies must disclose on these points even when the disclosure is negative.

Sample size

In this study, no specific sample size was determined for performing the ring-closing metathesis, either for in vitro or in vivo experiments. Screening of the artificial metathase at influential amino acid residues, as well as random residues (generated by error-prone PCR) was conducted. This process identified the artificial metathase variants that exhibited enhanced binding affinity to the designed cofactor and improved catalytic turnover numbers in the ring-closing metathesis.

Data exclusions

No data were excluded.

Replication

Data presented in the manuscript were performed in triplicates or more. Data collected in the Supplementary Information were performed in one or more replicates. All replication experiments were successful.

Randomization

Site-directed and site-saturation mutagenesis libraries of artificial metathase were generated by targeting the amino acid residues that are in proximity to the metal cofactor. Random mutagenesis libraries were generated by error-prone PCR and DNA fragment shuffling. For the site-directed mutagenesis clones, colonies with the correct mutational sequences were processed for protein expression and subsequent catalytic experiments. For the site-saturation and random mutagenesis libraries, mixed plasmids were used. During the screening process, colonies were randomly selected for enzyme expression. Only those variants with improved catalytic turnover numbers were sequenced, and the corresponding variants were selected for further characterization.

Blinding

No blind experiments were performed in this work as this is not a general procedure in the field.

Reporting for specific materials, systems and methods

We require information from authors about some types of materials, experimental systems and methods used in many studies. Here, indicate whether each material, system or method listed is relevant to your study. If you are not sure if a list item applies to your research, read the appropriate section before selecting a response.

	_	
	_	
9	ш	
	=	
g		
	T	
	٦	
7		
	≍	
- (\cup	
- 9		c
	$\overline{}$	Г
(ب	
		i
(\neg	
	$\boldsymbol{\smile}$	
-		
	_	
	ī	
. (7	1	
	T T	
700		
	TOO (
	Š	
(Š	
(Š	
(Š	
(
0	Š	
0		
9		
0		
0		
0		
0		
0		

S	
<	
S	

Materials & experimental systems		Methods	
n/a	Involved in the study	n/a Involved in the study	
\boxtimes	Antibodies	ChIP-seq	
\boxtimes	Eukaryotic cell lines	Flow cytometry	
\boxtimes	Palaeontology and archaeology	MRI-based neuroimaging	
\boxtimes	Animals and other organisms	·	
\boxtimes	Clinical data		
\boxtimes	Dual use research of concern		